Surface study by x-ray scattering technique and phase contrast imaging: the examples of graphene and sapphire

T.S. Argunova [1]✉ iD **, V.G. Kohn** [2] iD **, B.S. Roshchin** [2] iD **, A.D. Nuzhdin** [2] iD **,**

J.H. Lim [3] **, S.P. Lebedev** [1] iD **, A.V. Ankudinov** [1] iD

[1] Ioffe Institute, Saint-Petersburg, Russia

[2] National Research Centre "Kurchatov Institute", Moscow, Russia

[3] Pohang Accelerator Laboratory, Pohang, South Korea

✉ argunova2002@mail.ru

ABSTRACT
Nano-roughness evaluation for the surface of epitaxial graphene and height measurement are considered for a microstep on as-grown surface of sapphire in order to provide homogeneous graphene films on large areas of silicon carbide or sapphire substrates. To investigate dissimilar surface properties, different approaches have been used: off-specular grazing incidence X-ray scattering and in-line phase contrast imaging with synchrotron radiation. Statistical and local parameters of two types of surface morphology are measured. For the graphene surface, the dependence of the root-mean-square roughness of terrace-step nanostructure on the direction of the steps is estimated. For the vicinal face of sapphire, a surface step height of about one micron is determined directly from a phase contrast image, proving for the first time that the phase contrast imaging resolves surface morphology on a micrometer scale. Atomic force microscopy confirmed the obtained results.

KEYWORDS
graphene • epitaxial • SiC • sapphire ribbons • X-ray scattering • phase contrast imaging • synchrotron radiation

Introduction

Silicon carbide (SiC) and sapphire (Al$_2$O$_3$) substrates are widely used for epitaxial films and thin coatings. Substrate production requires the use of complex processing to obtain a smooth surface with standard roughness parameters (root mean square roughness, RMS; mean height of peaks; mean depth of valleys, etc.). Nevertheless, a residual damage layer remains on the substrate surface and its removal leads to the formation of terrace-step nanostructures (TSN). Thus, both flat and TSN surfaces are specific to SiC and Al$_2$O$_3$ depending on their processing. The fabrication of high-quality graphene by the thermal decomposition of SiC meets requirements on cleaning and annealing of substrate. The removal of the residual damaged layer results in TSN. The formation of a continuous graphene sheet on such a substrate may be a serious problem [1]. Chemical vapor

deposition (CVD) offers an alternative possibility to synthesize graphite films on Al_2O_3 substrates at elevated temperature. According to some authors [2], CVD films demonstrate improved electrical parameters compared to epitaxial graphene on SiC.

When making single-layer graphene on a substrate containing TSN, one should consider the minimum step height and maximum terrace width at the lowest surface roughness values. During thermal processing, the graphene sheet partly repeats the TSN pattern on the substrate. Moreover, single- and few-layer graphene grow on the same substrate leading to the formation of regions with different values of surface potential [3]. Increasing roughness, in turn, results in a spread in the electrical resistance of electronic devices (see, e.g., [4]). For example, in sensor chips that detect viruses, harmful gases, chemicals, etc., the conducting graphene channel is located between contact pads whose orientation does not correspond to that of the TSN. At the same time, the correlation between the root-mean-square roughness and the direction of steps is not yet clear.

Various methods can be suitable for the fabrication of graphene, each with its own advantages and substrate requirements. For instance, the synthesis of graphene on sapphire reduces the cost of purchasing substrates. The main benefit of the Stepanov–LaBelle technology over those for growing large sapphire crystals is the production of finished substrates. In particular, basal-faceted sapphire ribbons do not require the use of machining and finishing processes. The ribbons can serve as substrates for GaN, Ga_2O_3 or graphene. Wide and thin ribbons which can be used to epitaxially grow these materials still have structural defects. The defects include microsteps arising due to small differences in the ribbon thickness or deflection of its surface from the basal face.

In this work, grazing-incidence X-ray scattering (GIXS) measurements and phase contrast imaging (PCI) using Synchrotron Radiation (SR) have been employed to investigate the nano- and microscale morphology of graphene and sapphire. Specular reflectometry and off-specular X-ray scattering technique allow roughness, density and thickness determination in extremely thin surface layers. Spectral data processing and inverse problem solution are based on the theories of grazing incidence X-ray methods (see, e.g., [5–10]). Particularly, off-specular GIXS provides an opportunity to determine Power Spectral Density (PSD) function, which is directly associated with the statistical parameters of roughnes [10–13].

X-ray phase contrast imaging has become widespread due to the construction of 3rd–generation SR sources [14,15] and to upgrades of existing ones. In the setup of PCI, SR propagates through the sample and illuminates the volume within the field of view. When a local phase shift caused by small changes in electron density is variable over the beam cross-section, the corresponding intensity variation can be detected through the phenomenon of refraction. Though this method was used to quantitatively analyze micro-inhomogeneities in crystals [16,17], its feasibility for quantitative surface imaging has not been demonstrated yet. It has recently been shown that PCI is applicable to thin composite layers [18] that may contain microcracks [19]; however, this method has only been employed for qualitative observations.

We emphasize that the quantitative aspects of using PCI for characterization of surface morphology have not been previously considered, but will now be addressed in this paper. In the next sections, two different experimental methods are briefly described. X-ray scattering measurements near the critical angle for total external reflection of

epitaxial graphene are discussed. The results of imaging experiments on sapphire ribbons conducted at Pohang Light Source-II (PLS-II) are analyzed.

Materials and Methods

Semi-insulating SiC (0001) substrates purchased from different commercial channels had off-axis miscut angles, typically of the order of $\leq 0.2 - 2°$. The residual damaged layer was eliminated by high vacuum annealing in a closed tantalum cell in the temperature range of $1400 - 1500$ °C at a residual gas pressure of 10^{-4} Pa [20,21]. As a result, a fairly regular pattern of terraces separated by steps formed on the polar silicon (Si) face of SiC. A further increase in temperature to 1725 °C allowed us to obtain a graphene sheet in an area of ~ 1 cm^2. Graphene was formed under an argon (Ar) atmosphere at a pressure of $\sim 10^5$ Pa. The specific properties of graphene were confirmed by Raman spectroscopy.

Figure 1(a) shows a cross-section view of a typical multilayer graphene on 4H-SiC substrate obtained by high resolution transmission electron microscopy (HRTEM). An electron-transparent lamella was prepared by cutting the substrate, with the cutting line lay perpendicular to the step direction. It can be seen that the graphene is not uniform. A white line encircles the step on the substrate surface. The image shows a distinct feature located at the interface between the film and substrate, but we cannot distinguish a gap from a step on the film. Both types of these defects increase the surface roughness.
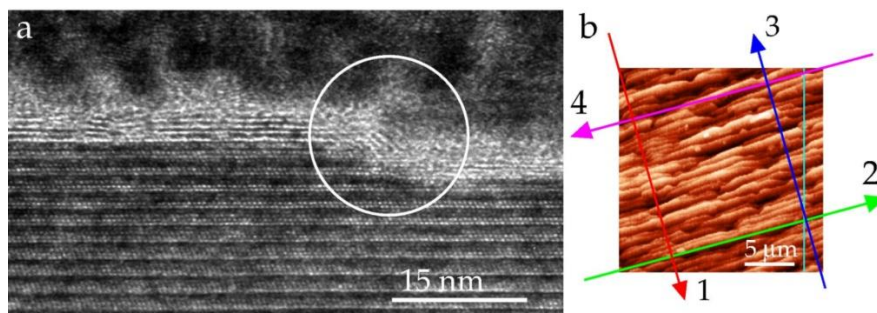

Fig. 1. (a) High resolution TEM image of the interface between Si-face 4H-SiC and multilayer graphene. White line encircles a step on the SiC surface; (b) AFM image of graphene surface. Arrows represent the X-ray scan directions, selected parallel (green, magenta) and perpendicular (red, blue) to the steps

The X-ray measurements were performed on a laboratory diffractometer [22]. A conventional X-ray tube with a Cu-anode served as a source. Radiation with wavelength $\lambda = 0.154$ nm reflected in a monochromator Si (111) within a passband of $\Delta\lambda/\lambda \approx 10^{-5}$. A vacuum collimator was placed between the sample and the detector to reduce parasitic scattering by air molecules. The collimated beam had a width of ~ 0.2 mm, a divergence of $\sim 10^{-4}$ rad and an intensity of $I \approx 3 \cdot 10^6$ c^{-1}. The initial position of the sample surface was horizontal and parallel to the direction of the incident beam. During X-ray measurements, the source and detector rotated around a stationary sample. A scintillation detector SCSD-4 (Radicon Ltd., St. Petersburg, Russia) was used in conjunction with a position-sensitive strip Dectris MYTHEN 2R (Dectris AG, Baden-Dättwil, Switzerland). The detectors provided good linearity and made it possible to measure the intensities of specularly reflected and scattered radiation in one process. Angular scanning varied between 0° and

3°; the direction of incidence was fixed by the angle 0.236°; the scattering transfer vector and spatial frequency were in the range of 0–0.42 Å^{-1} and 0.05–10 μm^{-1}, respectively. When the direct beam width in the plane of detector was 20 μm, the beam spot width on the sample was 5 mm at a grazing angle of 0.236°. The GIXS methodology for estimating TSN parameters was previously developed using Al$_2$O$_3$ and SiC substrates [23–25].

Compared to GIXS, PCI setup is very simple. Apart from the SR source, sample and detector, nothing else is required, provided that the spatial coherence of the incoming beam is sufficient. PCI is an appropriate technique to use, when a surface step entails a detectable phase shift. Since only intensities are measured, analytical means are needed to regain the phase-related information. Several efficient phase retrieval algorithms were produced.

The PCI experiments were carried out at the PLS-II operating at an electron energy of 3.0 GeV. At the BL6C beamline, a wiggler with a strong magnetic field (2.0 T) provides SR in the spectral range E = 23–50 keV. At a given energy of E = 23 keV, the double crystal monochromator selected a bandwidth $\Delta E/E$ = 2.9·10^{-4}. To obtain X-ray images, a sapphire ribbon was placed in the beam with its basal face perpendicular to the beam direction at a distance of r_s = 36 m from the wiggler source. Images were recorded with a scintillator screen coupled to a digital detector [26] located at a distance of r_d = 8 mm or 20 cm from the sample. Magnifying light optics projected a luminescent image onto the pixelated detector, and high image resolution was ensured by the small pixel size. In particular, the detector was equipped with a CCD matrix PCO Edge (PCO AG, Kelheim, Germany). Each chip had a resolution of 2560 × 2160 pixels and a size of 6.5 × 6.5 μm^2. The combination of ×20 objective lense with the PCO matrix led to an effective pixel size of 0.325 μm and a view field of 832 × 702 μm^2. For each pixel, a 16 bit analogue digital conversion was available.

Statistical parameters of roughness of epitaxial graphene on SiC

A characteristic feature within our approach is the computation of PSD function from angular distribution of scattered X-ray radiation [11–13]. The integral of the PSD function gives the effective roughness height σ_{eff}. The σ_{eff} is determined in the region of spatial frequencies limited by the width of the X-ray beam on one side and by the beam intensity on the other. In our case, the frequency range is limited by values v_{min} = 0.05 μm^{-1} and v_{max} = 10 μm^{-1}.

X-rays illuminate large surface areas; actually, the entire sample area (up to 25–30 mm, when the width of the direct beam in the detector plane is ~ 100 μm), therefore GIXS technique can detect high σ_{eff} values. An increase in the average roughness height leads to a significant increase in the PSD-function values. Atomic force microscopy (AFM) scan size is usually lower than 100 × 100 μm^2. Nevertheless, AFM has higher resolution, therefore this method can image finer roughness scales. With this approach, a probed area is approximately three orders of magnitude smaller. One can characterize the roughness scales by comparing the values of the PSD functions calculated from GIXS and AFM data.

Figure 1(b) is an AFM image of TSN on the surface of a multilayer graphene film. The image shows X-ray scan directions relative to the step edges. Colored lines numbered 1 and 3 indicate two parallel scans located perpendicular to the step edges. In Fig. 2 the

red (1) and blue (3) markers represent the PSD-curves plotted against frequency for scans 1 and 3, respectively. In the same diagram, the PSD-plots 2 and 4, shaped by green and magenta markers, refer to directions 2 and 4, which are parallel to the step edges. Note a peak in functions 1 and 3 that occurs when the beam scan is directed perpendicular to the steps. The position of the peak on the abscissa axis corresponds to the spatial frequency of the average TSN period. The peak shape is approximated by a Gaussian. The spread of periods and uneven edges of the terraces increase the peak width. The period value estimated from the GIXS data is 2.96 µm, but it should be noted that this result is obtained by averaging over a surface area of ~ 1 cm^2 illuminated by the beam. Scanning with a 90° rotation results in smoothing of the peak, as in the case of functions 2 and 4.
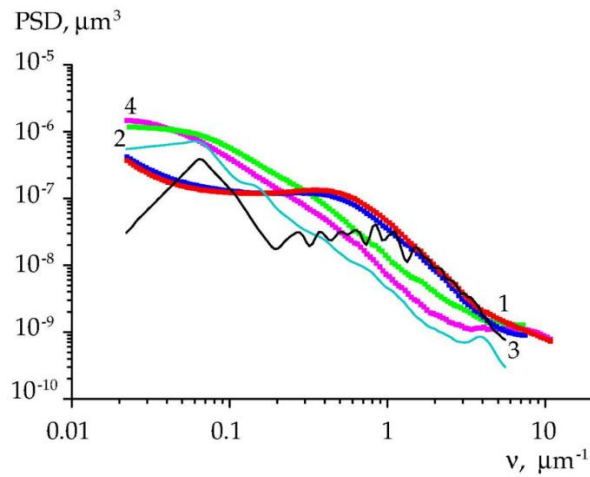

Fig. 2. Roughness PSD functions for multilayer graphene on Si face of 4H SiC. Plots corresponding to different scan directions are represented by markers of different colors: green, magenta (parallel) and red, blue (perpendicular) to the steps of TSN, respectively. PSD functions derived from AFM scans across (black) and along (cyan) the steps are indicated by curves without markers

In Fig. 2, solid lines (without markers) correspond to AFM scans directed along (cyan) or across (black) the steps, respectively. The behaviors of these PSD curves depending on the calculation direction are similar to those obtained with GIXS. Particularly, calculations across or along the steps result in a broad peak or monotonic decline, respectively. The discrepancy is seen in the low frequency region. The reason for the discrepancy relates to the decrease in AFM resolution that occurs when the roughness period is close to the AFM scan size. It should be stressed that in case of SiC substrates, a better match was obtained between the GIXS and AFM curves [25].

The effective roughness height σ_{eff} can be determined by the equation:

$$\sigma_{eff} = \sqrt{\int_{v_{min}}^{v_{max}} PSD\,(v)dv}.$$

The value of σ_{eff} extracted from PSD curves I–IV for directions 1–4 is: $\sigma_{eff}^{(1)} = 0.37$ nm, $\sigma_{eff}^{(2)} = 0.35$ nm, $\sigma_{eff}^{(3)} = 0.35$ nm, $\sigma_{eff}^{(4)} = 0.31$ nm. Thus, we see that the deviation (calculated as the arithmetic mean of the absolute values of the deviations) does not exceed 17 %. According to various researchers who have measured the root-mean-square roughness of graphene, these values are unlikely to result in a noticeable variation in electrical resistance.

Local step height on as-grown surface of sapphire

As described in the previous section, spatially averaged X-ray scattering gives the root-mean-square roughness of the entire sample area (e.g. ~ 1 cm^2). In this section we have again used the interaction of X-rays with matter, but in a different approach, which has the essential advantage of ensuring locality of measurements. The ensemble of local measurements constitutes an image. The image shows contrast due to changes in absorption, phase, or Bragg diffraction. Here we present X-ray phase contrast. The PCI setup provides a relatively limited field of view – from a few square millimeters to fractions of a millimeter. Nevertheless, the method combines localization and a fairly large area by moving the sample in front of the detector and recording images [27]. Since PCI cannot display morphology in a way similar to AFM, the latter is used in this work to obtain additional information about a surface structure.
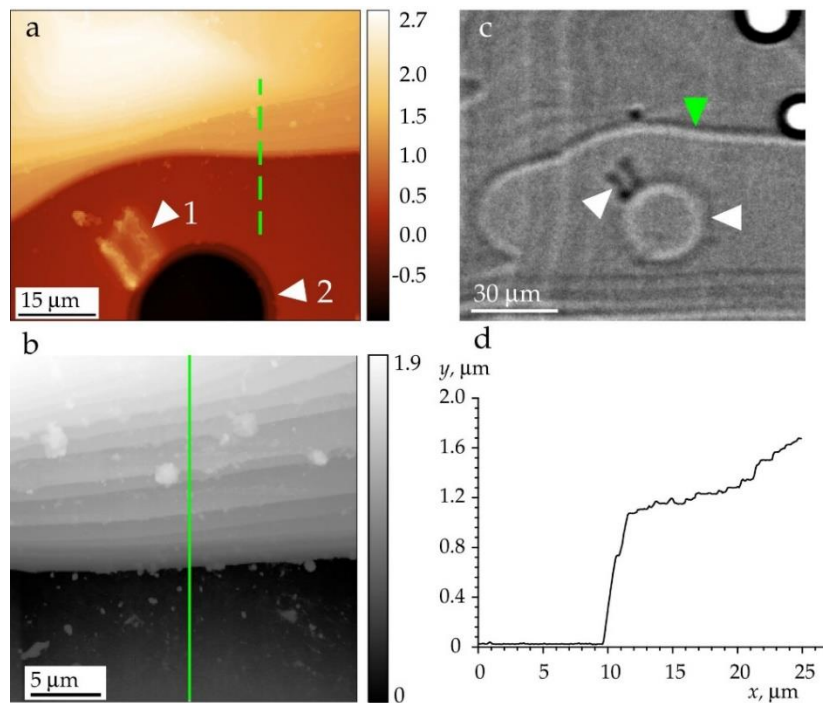

Fig. 3. (a) 2D representation of AFM data showing various defects in the sample. White arrows point to a particle (1) and a pit (2). The green dashed line indicates the AFM probing direction across the surface step. (b) AFM map of the step location. The solid line stands for the probing direction, identical to that shown in (a). In the phase contrast image (c), the green arrow points to the step region probed by AFM. White arrows point to the same features as in (a). Profile (d) of the step height (y, μm) vs. the distance across the step (x, μm)

Figure 3 contains AFM and PCI images of the sapphire ribbon grown from the melt using Stepanov's method at a growth rate of 1 mm/min up to a size of 10 × 0.4 × 100 (W×H×L) mm^3. The misorientation of the ribbon surface relative to the basal facet was only a few arc minutes. Figure 3(a) shows several defects imaged by AFM. At the bottom of the figure, one can see a rounded pit and an irregularly shaped defect in the vicinity of the pit. In the 3D representation of the AFM data, this defect appears as a particle (data not shown). The wavy line dividing the light and dark areas defines a step on the surface of

the ribbon. Green dashed line is for AFM scan across the step. The same scan is shown by the solid line in Fig. 3 (b), which displays a large-scale AFM map of the step location. At the top of the map, the light contrast corresponds to the step, and the dark contrast at the bottom comes from the material underneath the step. Furthermore, in the phase image (Fig. 3(c)) the same surface step is represented by a wavy line of black and white contrast. The green arrow indicates the position of the AFM scan on the sample surface. Note that the same location was chosen for the contrast evaluation on the phase image.

The pit and particle indicated above are present inside the region of interest. They were used as markers to localize both AFM and PCI measurements. We assume the following scenario for their formation. When a ribbon is pulled out, the metallic shaper heats up to a high temperature. A molten droplet can fall on the ribbon at some distance from the crystallization front, and overheating of the surface will lead to the formation of a pit.
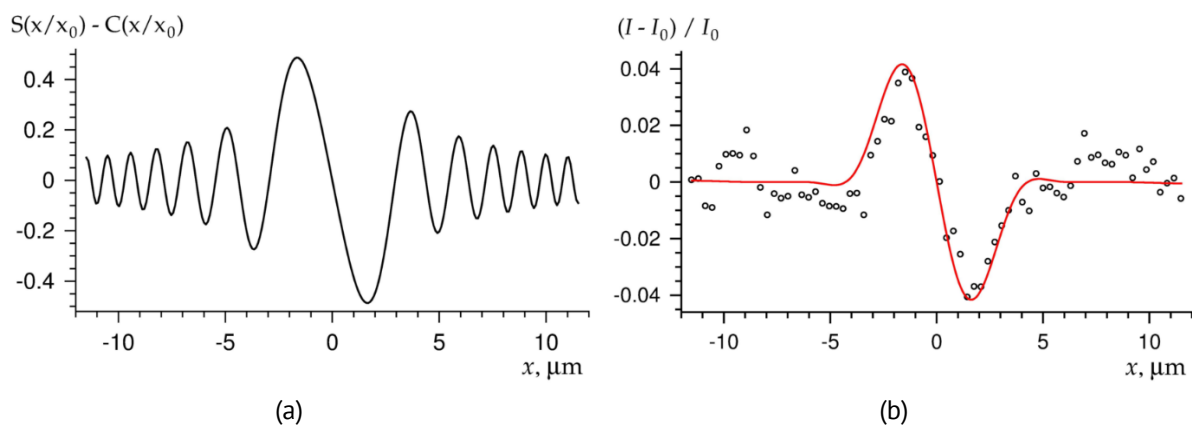

(a)

(b)

Fig. 4. Intensity profiles vs. the distance across the surface step. (a) Theoretical profile calculated for coherent radiation from a point source. $x_0 = 2.32$ μm. (b) Experimental (open circles) and theoretical (smooth red curve) relative intensity distributions. The red curve is obtained by averaging the profile in (a) after convolution with a Gaussian function (FWHM is 3 μm)

To evaluate theoretical intensity distribution for the step we employed X-Ray Wave Propagation (XRWP) computer program [28]. The result obtained for a point source and fully coherent radiation is shown in Fig. 4(a), where the maximum is located on the side of the smaller sample thickness. We note that many Fresnel fringes are formed besides the maximum and minimum.

The experimental profile was obtained by measuring the contrast of the phase image recorded in a CCD (Fig. 3(c)). The image was stored in TIFF format, 16-bit. TIFF file was converted into a matrix. In the course of further processing, the matrix was used to produce the image of the step with highest possible contrast. The intensity was measured perpendicular to the step section. Here we want to emphasize again that the section was located within the region of the AFM scan (Fig. 3(a)). In Fig. 4(b) open circles stand for the experimental data. One can see that the Fresnel fringes are simply not detected.

The theoretical and experimental intensity distributions were compared. Prior to the comparison, averaging on the fringes was performed. As an averaging method we propose to employ the standard convolution with a Gaussian function. The method is successful in cases when the factors responsible for the reduction in spatial coherence are unspecified. The full width at half maximum (FWHM) of Gaussian can be determined

from preliminary experiments on test objects [29,30]. Finally, the smoothed theoretical profile is drawn by the red line in Fig. 4(b) (FWHM of the Gaussian is 3 μm).

Analytical solution gives the same results in a much more simple way. When the phase shift ϕ introduced by a surface step is small compared to unity, the intensity profile can be calculated as a power series of ϕ. Retaining only the first dominant contribution, we conclude that the contrast is proportional to ϕ, and the intensity profile is calculated analytically using an equation:

$$I/I_0 = 1 + \phi[S(x/x_0) - C(x/x_0)], \ \phi = K\delta t, \ x_0 = (\lambda r_d/2)^{1/2}, \tag{1}$$

where $S(x)$ and $C(x)$ are the sine and cosine Fresnel integrals, r_d is the distance from the object to the detector, ϕ is the local phase shift introduced by the step; $\phi << 1$. The contrast of the step determined from the plot is 0.2ϕ. Using the estimation of phase $\phi = 0.2$, obtained from the comparison of the experimental and simulated contrasts, and the decrement of the refractive index of sapphire $\delta = 1.532 \cdot 10^{-6}$, we find the step height t from the Eq. (1): $t = 1.12$ μm. This value is confirmed by the AFM data. The AFM analysis, whose graphical result is presented in Fig. 3(d), gives the step height versus the distance across the step. One can see that the step height changes slightly from 1 to 1.5 μm.

Conclusions

The present study is an example of the application of grazing-incidence X-ray scattering technique and phase contrast imaging to graphene and sapphire. The quality of graphene surface was estimated by statistical parameters of roughness. The surface of sapphire was investigated by in-line PCI method, which did not yet deal with solid surfaces and crystal faces. The novelty in the PCI experiment is that the microstep height has been determined directly from an image with fairly good accuracy (~ 1 μm), despite the relatively large decrease in spatial coherence. Our experimental design involves techniques that are not feasible in the same setup. Nevertheless, the combination of X-ray-matter interactions, namely scattering and refraction, which are commonly used for different purposes, has led to a better interpretation of surface morphology.

References

1. Yakimova R, Virojanadara C, Gogova D, Syväjärvi M, Siche D, Larsson K, Johansson LJ. Analysis of the formation conditions for large area epitaxial graphene on SiC substrates. *Materials Science Forum.* 2010;645–648: 565–568.

2. Shan J, Sun J, Liu Z. Chemical vapor deposition synthesis of graphene over sapphire substrates. *ChemNanoMat.* 2021;7(5): 515–525.

3. Mammadov S, Ristein J, Krone J, Raidel C, Wanke M, Wiesmann V, Speck F, Seyller T. Work function of graphene multilayers on SiC(0001). *2D Mater.* 2017;4(1): 015043.

4. Shmidt NM, Shabunina EI, Gushchina EV, Petrov VN, Eliseyev IA, Lebedev SP, Priobrazhenskii SI, Tanklevskaya EM, Puzyk MV, Roenkov AD, Usikov AS, Lebedev AA. Quality assessment of processed graphene chips for biosensor application. *Materials.* 2023;16(16): 5628(1–10).

5. Vinogradov AV, Zorev NN, Kozhevnikov IV, Yakushkin IG. Phenomenon of total external reflection of X–rays. *Sov. Phys. JETP.* 1985;62(6): 1225–1229.

6. Kozhevnikov IV, Asadchikov VE, Alaudinov BM, Karabekov AYu, Vinogradov AV. X-ray investigations of supersmooth surfaces. In: *Proceedings of X-ray Optics and Surface Science.* 1995. p. 141–153.

7. Stoev KN, Sakurai K. Review on grazing incidence X-ray spectrometry and reflectometry. *Spectrochimica Acta Part B.* 1999;54(1): 41–82.

8. Zhou X-L, Chen S-H. Theoretical foundation of X-ray and neutron reflectometry. *Physics Reports.* 1995;257(4–5): 223–348.

9. Andreev AV. Theory of X-ray scattering by rough surfaces without distorted wave approximation. *Phys. Lett. A.* 1996;219(5–6): 349–354.

10. Kozhevnikov, IV, Pyatakhin MV. Use of DWBA and perturbation theory in X-ray control of the surface roughness. *J. X-Ray Sci. Technol.* 1998;8(4): 253–275.

11. Kozhevnikov IV. Physical analysis of the inverse problem of X-ray reflectometry. *Nucl. Instrum. Methods Phys. Res. A.* 2003;508(3): 519–541.

12. Asadchikov VE, Kozhevnikov IV, Krivonosov YS, Mercier R, Metzger TH, Morawe C, Ziegler E. Application of X-ray scattering technique to the study of supersmooth surfaces. *Nucl. Instrum. Meth. Phys. Res. A.* 2004;530(3): 575–595.

13. Kozhevnikov IV. General laws of x-ray reflection from rough surfaces: II. Conformal roughness. *Crystallogr. Rep.* 2012;57: 490–498.

14. Snigirev A, Snigireva I, Kohn V, Kuznetsov S, Schelokov I. On the possibilities of x-ray phase contrast microimaging by coherent high-energy synchrotron radiation. *Rev. Sci. Instrum.* 1995;66(12): 5486–5492.

15. Cloetens P, Barrett R, Baruchel J, Guigay JP, Schlenker M. Phase objects in synchrotron radiation hard x-ray imaging. *Journal of Physics D.* 1996;29(1): 133–146.

16. Kohn VG, Argunova TS, Je JH. Study of micropipe structure in SiC by x-ray phase contrast imaging. *Appl. Phys. Lett.* 2007:91(17); 171901.

17. Argunova TS, Kohn VG. Study of micropores in single crystals by in-line phase contrast imaging with synchrotron radiation. *Physics-Uspekhi.* 2019;62(6): 602–616.

18. Yeager JD, Luo SN, Jensen BJ, Fezzaa K, Montgomery DS, Hooks DE. High-speed synchrotron X-ray phase contrast imaging for analysis of low-Z composite microstructure. *Composites Part A.* 2012;43(6): 885–892.

19. Ignateva EV, Krasnitckii SA, Sheinerman AG, Gutkin MYu. The finite element analysis of crack tolerance in composite ceramics. *Materials Physics and Mechanics.* 2023;51(2): 21–26.

20. Dunaevskii MS, Makarenko IV, Petrov VN, Lebedev AA, Lebedev SP, Titkov AN. Using atomic-step-structured 6H-SiC(0001) surfaces for the calibration of nanotranslations in scanning probe microscopy. *Tech. Phys. Lett.* 2009;35(1): 47–49.

21. Lebedev SP, Petrov VN, Kotousova IS, Lavrentev AA, Dementev PA, Lebedev AA, Titkov AN. Formation of periodic steps on 6H-SiC (0001) surface by annealing in a high vacuum. *Mater. Sci. Forum.* 2011;679–680: 437–440.

22. Asadchikov VE, Babak VG, Buzmakov AV, Dorokhin YP, Glagolev IP, Zanevskii YV, Zryuev VN, Krivonosov YS, Mamich VF, Moseiko LA, Moseiko NI, Mchedlishvili BV, Savel'ev SV, Senin RA, Smykov LP, Tudosi GA, Fateev VD, Chernenko SP, Cheremukhina GA, Cheremukhin EA, Chulichkov AI, Shilin YuN, Shishkov VA. An X-ray diffractometer with a mobile emitter-detector system. *Instrum. Exp. Technol.* 2002;48(3): 364–372.

23. Butashin AV, Muslimov AE, Kanevsky VM, Deryabin AN, Pavlov VA, Asadchikov VE. Structural contribution to the roughness of supersmooth crystal surface. *Cryst. Rep.* 2013:58(3): 483–487.

24. Asadchikov VE, Blagov AE, Butashin AV, Volkov YO, Deryabin AN, Kanevskii VM, Muslimov AE, Protsenko AI, Roshchin BS, Targonskii AV, Chukhovskii FN. Lateral inhomogeneities of sapphire plates determined with the aid of x-ray and probe methods. *Technical Physics.* 2020;65(3): 400–406.

25. Roschin BS, Argunova TS, Lebedev SP, Asadchikov VE, Lebedev AA, Volkov YO, Nuzhdin AD. Application of grazing-incidence X-ray methods to study terrace-stepped SiC surface for graphene growth. *Materials.* 2022;15(21): 7669(1–13).

26. Bonse U, Busch F. X-ray computed microtomography using synchrotron radiation. *Prog. Biophys. Mol. Biol.* 1996;65(1–2): 133–169.

27. Argunova TS, Kohn VG, Lim J-H, Krymov VM, Gutkin MYu. Large-area mapping of voids and dislocations in basal-faceted sapphire ribbons by synchrotron radiation imaging. *Materials.* 2023;16(19): 6589.

28. Kohn VG. Available online: https://xray-optics.ucoz.ru/XR/xrwpe.htm (accessed on 08 October 2024).

29. Kohn V, Snigireva I, Snigirev A. Interferometric characterization of spatial coherence of high energy synchrotron X-rays. *Optics Communications.* 2001;198(4-6); 293–309.

30. Argunova TS, Kohn VG, Lim J-H, Krymov VM, Ankudinov AV. Imaging of micro-steps on as-grown surface of sapphire with X-ray phase contrast technique. *Physics Letters A.* 2024;525: 129901(1–4).

About Authors

Tatiana S. Argunova ⓘ Sc

Doctor of Physical and Mathematical Sciences
Chief Researcher (Ioffe Institute, Saint-Petersburg, Russia)

Victor G. Kohn ⓘ Sc

Doctor of Physical and Mathematical Sciences
Chief Researcher (National Research Centre "Kurchatov Institute", Moscow, Russia)

Boris S. Roshchin ⓘ Sc

Candidate of Physical and Mathematical Sciences
Researcher (National Research Centre "Kurchatov Institute", Moscow, Russia)

Alexander D. Nuzhdin ⓘ Sc

Junior Researcher (National Research Centre "Kurchatov Institute", Moscow, Russia)

Jae-Hong Lim Sc

Beamline Scientist (Pohang Accelerator Laboratory, Pohang, South Korea)

Sergey P. Lebedev ⓘ Sc

Candidate of Physical and Mathematical Sciences
Senior Researcher (Ioffe Institute, Saint-Petersburg, Russia)

Alexander V. Ankudinov ⓘ Sc

Candidate of Physical and Mathematical Sciences
Senior Researcher (Ioffe Institute, Saint-Petersburg, Russia)